Origin of giant enhancement of phase contrast in electron holography of modulation-doped *n*-type GaN

K. Ji [a,b], M. Schnedler [a], Q. Lan [a], J.-F. Carlin [c], R. Butté [c], N. Grandjean [c], R.E. Dunin-Borkowski [a,b], Ph. Ebert [a,*]

[a] *Ernst Ruska Centrum (ER-C-1) and Peter Grünberg Institut (PGI-5), Forschungszentrum Jülich GmbH, Jülich, 52425, Germany*
[b] *Institut für Experimentalphysik IV E, RWTH Aachen University, Aachen, 52056, Germany*
[c] *Institute of Physics, Ecole Polytechnique Fédérale de Lausanne, Lausanne, 1015, Switzerland*

ARTICLE INFO

ABSTRACT

The electron optical phase contrast probed by electron holography at n-n^+ GaN doping steps is found to exhibit a giant enhancement, in sharp contrast to the always smaller than expected phase contrast reported for p-n junctions. We unravel the physical origin of the giant enhancement by combining off-axis electron holography data with self-consistent electrostatic potential calculations. The predominant contribution to the phase contrast is shown to arise from the doping dependent screening length of the surface Fermi-level pinning, which is induced by FIB-implanted carbon point defects below the outer amorphous shell. The contribution of the built-in potential is negligible for modulation doping and only relevant for large built-in potentials at e.g. p-n junctions. This work provides a quantitative approach to so-called dead layers at TEM lamellas.

1. Introduction

Electron beam based microscopy techniques, such as 4D scanning transmission electron microscopy (4D-STEM) [1–3], electron beam-induced current (EBIC) [4,5], and scanning electron microscopy (SEM) [6–9], have been frequently utilized to map and quantify electrostatic potentials in semiconductors at high spatial resolution. Among all techniques, electron holography in a transmission electron microscope (TEM) turned out to be the method that provides highest energy precision at nm scale resolution, while minimizing electron beam induced damage to the sample. The benefits and limitations of this methodology for quantifying electrostatic potentials have been primarily demonstrated using p-n junctions [10–23] and more recently ternary heterointerfaces and doping steps [24–28]. The intriguing conclusions from these previous studies are that the electron optical phase contrast across a p-n junction is always smaller than anticipated, whereas the phase contrast across a, e.g. n-n^+, doping step is larger than expected. In addition, the phase contrast across a p-n junction increases with the lamella's thickness [10,14–16,18–21,29–31], while such effects have not been reported yet for doping steps. How can we understand these differences?

Solving this issue raises the question of the physical origin of the phase contrast in electron holography of doping structures. In this paper we probe the electron optical phase change across an n-n^+ doping step using off-axis electron holography in transmission electron microscopy. We find a phase contrast about one order of magnitude larger than expected. The giant phase contrast enhancement is shown to arise from the doping dependence of free-carrier screening of the surface potential of the TEM lamellas. For different doping regions, this gives rise to varying widths of screening layers, which are dominating the contrast. The phase contrast contribution of the built-in potential, which is dominating for p-n junctions, is negligible for doping steps.

2. Experimental procedures

As model system we use an n-n^+ doping step in GaN with Si concentrations of 8×10^{17} and 3.5×10^{18} cm^{-3}, respectively, as determined by secondary ion mass spectrometry (SIMS). The TEM lamellas were prepared using focused ion beam (FIB) milling in a FEI Helios NanoLab 460F1 instrument. Prior to FIB milling, the bulk semiconductor sample is first 5 kV e-beam coated with a 100 nm carbon layer, followed by a 2 μm C protective layer, deposited using a 30 kV Ga ion beam, with $C_{10}H_8$ as precursor. A 2–3 μm thick lamella is then cut from the sample using 30 kV Ga ions at 85° relative to the surface plane. Subsequently, the lamella is attached with carbon to a TEM grid and thinned to ~1700 nm using a 30 kV Ga$^+$ ion beam with a grazing incidence angle of 2° relative to the surface. Further thinning proceeds with progressively reduced ion dose and incidence angle until

---

a thickness of approximately 400 nm is reached. The final polishing process is conducted using 5 kV Ga$^+$ with an ion dose of 16 pA and at 5° grazing incidence angle. The crystalline thicknesses t of the lamellas is determined utilizing the convergent beam electron diffraction (CBED) technique [32].

The FIB-prepared lamellas are investigated by off-axis electron holography in a TEM (FEI Titan G2 60–300 HOLO, FEI instrument) operated at 300 kV [33]. The upper biprism is biased at 120 V giving a proper field-of-view and a high contrast of the interference patterns. The lamella is kept at edge-on orientation and tilted away from the [10$\bar{1}$0] zone axis to suppress the dynamical diffraction. Single-frame holograms are acquired with exposure time of 10–12 s, with a fringe spacing of 2–3 nm. Particular attention has been paid to extract phase change profiles from regions free of dynamic diffraction.

3. Results

An example of a phase map derived from a hologram acquired across GaN doping step is displayed in Fig. 1(a). The investigated lamella exhibits a crystalline thickness of $t = 257 \pm 6$ nm as measured by CBED. The [0001] growth direction points to the right. The GaN layer with lower donor concentration exhibits a darker contrast. The corresponding phase change profile, averaged over 500 nm width, is plotted in Fig. 1(b). The difference in phase across the doping step, denoted as $\Delta\phi_{junction}$, is found to be 0.40 ± 0.02 rad. Fig. 1(c) reports the $\Delta\phi_{junction}$ values measured from various lamellas with crystalline thicknesses ranging from 188 to 380 nm. A linear fit (blue line) reveals a weak slope of $(2.0 \pm 1.3) \times 10^{-4}$ rad/nm with an intercept of 0.33 ± 0.04 rad. The large intercept as well as the weak slope indicate an almost thickness independent phase contrast across the doping junction.

For quantitative interpretation of the measured phase change profiles, self-consistent electrostatic potential calculations are carried out, taking the presence of a surface Fermi-level pinning E_{pin} of the TEM lamellas into consideration. We recall, that the FIB preparation results in a lamella consisting of a pristine core, covered by a defect-rich crystalline inner shell and an amorphous outer shell [34]. The Fermi-level pinning has been shown to arise from a FIB-induced near surface implantation of carbon on nitrogen sites in the inner shell [34] (see for details in the discussion section below). The quantitative analysis of the measured phase change profiles is based on a two-step process: [24] First, the built-in electrostatic potential V_{bi} as well as the interaction between the FIB-induced surface potential and the free carriers is determined by using a self-consistent finite-difference based Poisson solver, as described in Refs. [35,36]. In a second step, the electron optical phase change map is calculated by integrating the obtained three-dimensional electrostatic potential along the electron beam direction [24].

In Fig. 1 (b), the measured phase change profile across GaN doping step is compared with calculated results, using E_{pin} as a fitting parameter. The red and blue lines represent calculated phase change profiles with a surface Fermi-level pinning of 0.69 and 0.59 eV above the valence band edge (E_V), respectively, while the green dashed line is derived assuming no pinning states at the surface, i.e. only bulk conditions.

For the unpinned surface, the phase contrast between the n and n^+-doped GaN $\Delta\phi_{bi}$ is only 0.04 rad. This value is solely originating from the built-in potential $V_{bi} = 26$ mV between differently doped n-type GaN layers, i.e. $\Delta\phi_{bi} = C_E \cdot V_{bi} \cdot t$ with $C_E = 0.00652$ rad V^{-1} nm^{-1} at 300 kV. Hence without surface consideration a phase contrast much smaller than observed would be expected.

With the presence of pinning states at the surfaces of the lamella, the phase contrast and $\Delta\phi_{junction}$ increase with E_{pin} shifting toward E_V. The best agreement between the experimental phase change profile shown in Fig. 1(b) and the calculated result is found for $E_{pin} = 0.69 \pm 0.1$ eV. In
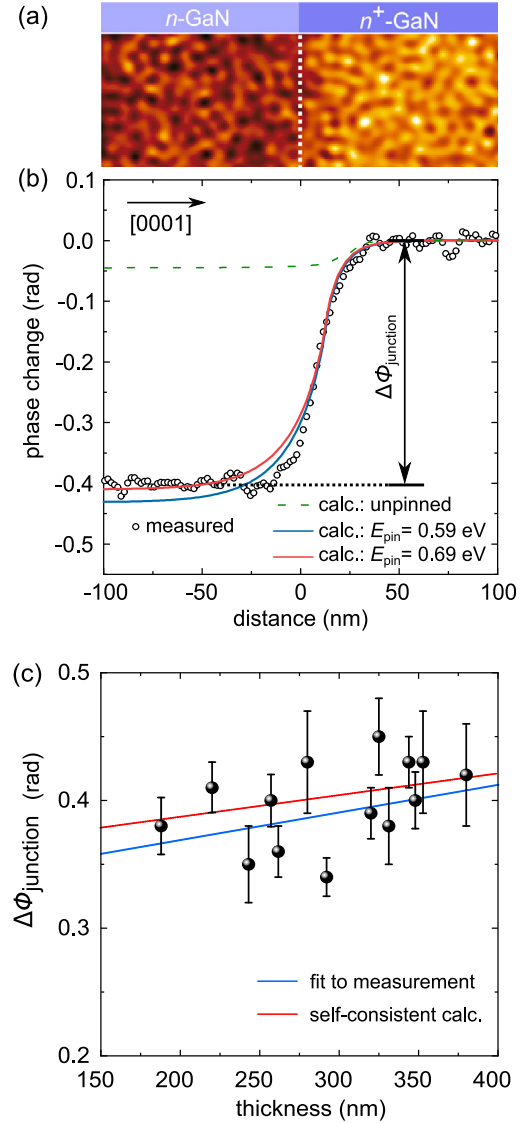

Fig. 1. (a) Phase map across an n-n^+ GaN doping step. The n-GaN layer exhibits a darker contrast. (b) Phase change profile extracted from the phase map averaged over a width of 500 nm. The n-n^+ interface is positioned at 0 nm. The phase contrast across the doping step $\Delta\phi_{junction}$ is 0.4 rad. (c) $\Delta\phi_{junction}$ versus crystalline thickness of the measured lamellas. The blue line represents a linear fit, whereas the red line is obtained from self-consistent electrostatic simulations.

order to provide a feeling for the accuracy of E_{pin} a second simulation with a pinning level 0.1 eV closer to E_V is illustrated.

The same analysis is performed for all lamellas. Fig. 2 illustrates the derived pinning levels E_{pin} vs. crystalline thickness (ranging from 188 to 380 nm) for all investigated 14 lamellas. A linear fit to the data reveals a constant average Fermi-level pinning energy independent of the lamella thickness with negligible slope [$(-1.2 \pm 5.5) \times 10^{-4}$ eV/nm]. The average value of E_{pin} of 0.70 ± 0.13 eV is in good agreement with values derived in our previous work on a delta-doped GaN layer of 0.69 ± 0.2 and 0.57 ± 0.05 eV [24,34].

4. Discussion

In order to gain more insight into the origin of the phase contrast as well as the interplay between lamella thickness and phase contrast across a GaN doping step, we turn to the calculated cross-sectional
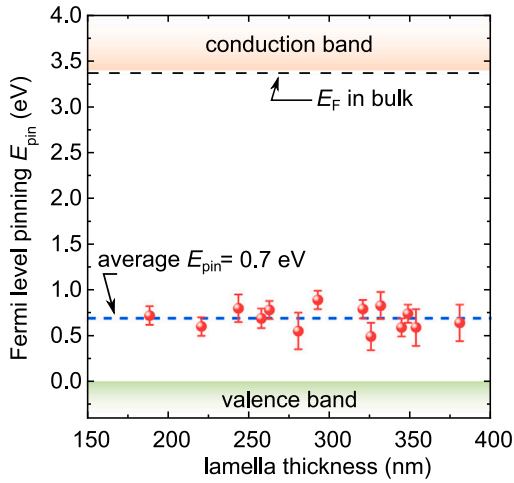
Fig. 2. Energy position of the Fermi-level pinning E_{pin} vs. crystalline thickness derived from all investigated FIB-prepared lamellas. An average E_{pin} of 0.70 ± 0.13 eV is revealed with no detectable thickness dependence.

electrostatic potential maps of lamellas with thicknesses of 330 nm [Fig. 3(a1)] and 260 nm [Fig. 3(b1)]. The surface Fermi-level is set to be pinned at 0.70 eV above the valence band edge. The potential profiles extracted along the $[10\bar{1}0]$ electron beam direction at the positions of the blue (red) dashed and solid lines are shown in Fig. 3(a2) [Fig. 3(b2)] below. Note, the incident electron beam direction points here from left to right.

The potential maps and line profiles reveal that the main potential difference between the n and n^+-doped GaN layers is found near the surfaces of the TEM lamella where the Fermi-level is pinned [vertical orange lines in Fig. 3 (a2) and (b2)]. In this region the surface potential is screened by the free charge carriers. Since the screening length is exponentially decreasing with carrier concentration [37,38], the extent of the depletion layer in significantly different for the n and n^+-GaN layer, i.e. ~63 vs.~32 nm, respectively. In contrast in the pristine crystalline core of the lamella the potential is almost identical for the different doping levels, since the built-in potential V_{bi} between the n and n^+-GaN layers is only 26 mV.

The potential profiles illustrate well that the biggest contribution to the difference in potential and thus phase is the depletion layer where screening of the surface potential takes place. This leads to phase contrasts in the order of 0.38 rad across the doping step. For comparison, the phase contrast stemming solely from the built-in potential ΔV_{bi} is so small that it can be almost neglected, since it is only ~0.04 rad for, e.g., the 260 nm thick lamella [Fig. 3 (b2)]. Thus, the predominant contribution to the phase contrast across the doping step arises from different (doping-dependent) screening lengths of the surface potential, and not from the built-in potential in the pristine crystalline core. This observation is reflected in Fig. 3(d) where the corresponding phase change profiles integrated through the whole lamella thickness, extracted from lamella A (blue line) and B (red line) are compared. Despite lamella A is 70 nm (~ 27%) thicker than lamella B, $\Delta\phi_{junction}$ is only 0.01 rad (~ 2.6%) higher.

The solid red line in Fig. 1 (c) illustrates the calculated $\Delta\phi_{junction}$ as a function of crystalline thickness. The thickness dependence is weak and almost linear and agrees well with the data points. This supports further the above physical conclusions, that for doping modulations the screening is governing the electron optical phase contrast.

The situation can be anticipated to change, if large built-in potentials occur, such as in p-n junctions or at heterointerfaces. The surface pinning shifts the Fermi-level toward mid-gap position for both, n- and p-type layers, reducing the built-in potential in the near surface region. Thereby a phase difference across the p-n junction is obtained, which is

always smaller than expected without surface potentials and dead shell layers.

As a side note, the FIB-induced amorphous outer shell layer is not accounted for in the calculation. The phase is obtained by integrating the electrostatic potential along the electron beam direction [39] within the crystalline part of the lamella, only. This approach is valid, since the amorphous shell is anticipated to be homogeneously intermixed everywhere leading to an equipotential surface. Furthermore, we anticipate that the amorphous shell is conductive, hence screening the surface potential toward the vacuum. This is supported by the absence of fringing fields in the vacuum near the lamella during experiments with our FIB-prepared TEM lamellas. Therefore, the amorphous shell is not contributing to the phase difference.

Finally, the defect rich crystalline inner shell is rather thin in our case. We can estimate its thickness by taking into account an average thickness of the amorphous shell of 9 nm and the carbon implantation profile obtained by transport range of ions in matter (TRIM) simulations. The TRIM simulations indicate, that the carbon concentration decays exponentially and falls at a depth of about 15–18 nm below the doping concentration [34]. This yields a thickness of about 6–9 nm where the carbon concentration exceeds the doping concentration and no screening occurs yet, as all dopants will be compensated. Hence, the material will be fully pinned and not contribute to the electron optical phase contrast. Only deeper inside the lamella screening occurs and dominates the phase contrast. Since in our case the defect-rich inner crystalline shell is rather thin as compared to the lamella thickness, it is sufficient to approximate its effect on the potential as a surface Fermi-level pinning.

Hence, we conclude that the quantitative analysis of phase differences measured by electron holography using FIB-prepared TEM lamellas, requires the consideration of more than simply a dead layer [12–16,18–21,27,29–31,40,41]. Instead, an amorphous outer shell, a defect-rich inner crystalline shell, and an underlying depletion region within the pristine crystalline core screening the surface potential need to be considered and evaluated for every material investigated. In particular one needs to understand the physics of FIB-induced point defects and their charge transfer levels, which determine the Fermi-level pinning.

The analysis methodology and self-consistent electrostatic potential calculation can be applied to earlier published data, too, to assess E_{pin}. However, the choice of examples is not straightforward, primarily because of the uncertainty associated with the lamella preparation in literature. Using a different FIB preparation process, such as employing different protective layers, applying heavier ion sources and higher ion voltage [14], can be anticipated to give rise to lamellas with different surface conditions.

The data set the closest to our experimental parameters is that of Yamamoto et al [25], where a protective carbon layer was used. The lift-out and initial thinning were performed using 40 kV Ga$^+$ ions, whereas the final polishing was conducted at 5 kV. The resulting lamella had a final thickness of 350 nm. An experimentally measured phase contrast of 0.55 ± 0.05 rad across an n-n^+ GaN doping step has been reported (Si doping of 5×10^{17} and 5×10^{18} cm^{-3}, respectively). The magnitude of phase difference is again in sharp contrast to the theoretical predictions without surface pinning of 0.14 rad (derived using a Poisson solver software, Aestimo, without considering surface defect effects) [42]. Applying the here derived surface pinning model to *their* measurement data yields a surface Fermi-level pinning of 0.84 ± 0.2 eV above E_V. This pinning value is in line with that obtained from *our* measurement data, i.e. E_{pin} of 0.70 ± 0.13 eV, indicating that the pinning near the valence band is a general property of FIB-prepared GaN lamellas with C protective layers.
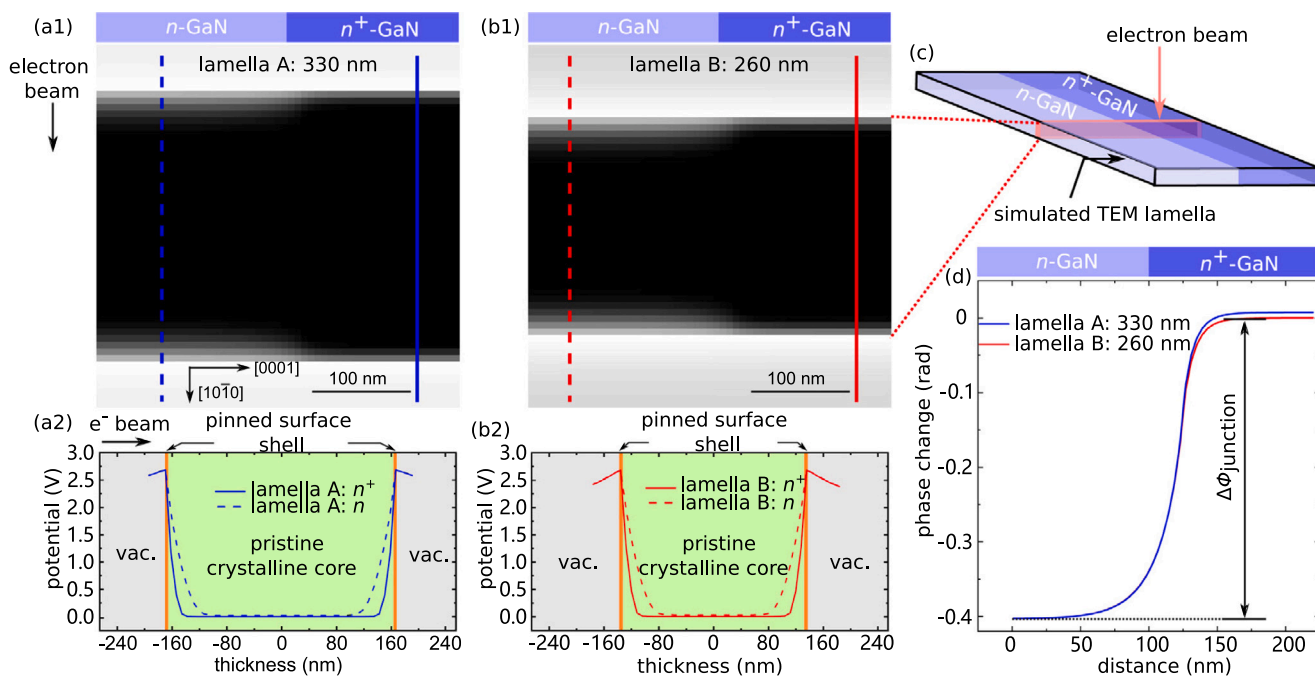
Fig. 3. (a1, b1) Simulated cross-sectional electrostatic potential maps of the same GaN n-n^+ doping step for TEM lamellas with a thickness of 330 nm (a1) and 260 nm (b1). (a2) Potential profiles extracted along the respective vertical dashed and solid lines in (a1). The vacuum and pristine crystalline core are visualized with gray and green background color, respectively. (b2) Same as (a2) but extracted from (b1). (c) Sketch of a TEM lamella of the n-n^+ GaN doping step showing the spatial positions of the potential maps in (a1, b1). (d) Comparison of phase change profiles calculated for lamellas with a crystalline thickness of 260 (red line) and 330 nm (blue line).

5. Conclusions

The electron optical phase contrast at n-n^+ GaN doping steps is shown to exhibit a giant enhancement as compared to expectations, with an almost negligible thickness dependence. The physical origin of the giant enhancement is unraveled by combining off-axis electron holography data with self-consistent electrostatic potential calculations. The predominant contribution to the phase contrast is shown to arise from the doping dependent screening length of the FIB-induced surface Fermi-level pinning occurring in the defect-rich crystalline inner shell (below the outer amorphous shell). This near surface depletion region remains unchanged for lamellas with different thicknesses, resulting in an almost constant electron optical phase contrast vs. thickness. The contribution of the built-in potential is almost negligible, since its value is too small for modulation doping and only relevant for large built-in potentials at e.g. p-n junctions. Thus, the weak built-in potential of GaN doping steps adds only a small thickness dependence to the phase contrast. This work dissects the previously termed dead layers to identify the defect-rich crystalline inner shell and the screening of its Fermi-level pinning being solely relevant for electron optical phase differences, thereby providing a quantitative approach to dead layers at surfaces of TEM lamellas.

CRediT authorship contribution statement

K. Ji: Writing – original draft, Visualization, Investigation, Formal analysis. **M. Schnedler:** Writing – review & editing, Supervision, Software. **Q. Lan:** Writing – review & editing, Supervision. **J.-F. Carlin:** Resources. **R. Butté:** Writing – review & editing, Resources. **N. Grandjean:** Writing – review & editing, Resources. **R.E. Dunin-Borkowski:** Funding acquisition, Writing – review & editing. **Ph. Ebert:** Writing – review & editing, Writing – original draft, Supervision, Conceptualization.

Declaration of competing interest

The authors declare that they have no known competing financial interests or personal relationships that could have appeared to influence the work reported in this paper.

Data availability

Data will be made available on request.

Acknowledgments

References

[1] K. Müller, F.F. Krause, A. Béché, M. Schowalter, V. Galioit, S. Löffler, J. Verbeeck, J. Zweck, P. Schattschneider, A. Rosenauer, Atomic electric fields revealed by a quantum mechanical approach to electron picodiffraction, Nat. Commun. 5 (1) (2014) 5653.

[2] K. Müller-Caspary, F.F. Krause, T. Grieb, S. Löffler, M. Schowalter, A. Béché, V. Galioit, D. Marquardt, J. Zweck, P. Schattschneider, et al., Measurement of atomic electric fields and charge densities from average momentum transfers using scanning transmission electron microscopy, Ultramicroscopy 178 (2017) 62–80.

[3] B.C. da Silva, Z.S. Momtaz, L. Bruas, J.-L. Rouviére, H. Okuno, D. Cooper, M.I. Den-Hertog, The influence of illumination conditions in the measurement of built-in electric field at p–n junctions by 4d-stem, Appl. Phys. Lett. 121 (12) (2022).

[4] A. Pugatschow, R. Heiderhoff, L.J. Balk, Quantitative determination of electric field strengths within dynamically operated devices using ebic analysis in the sem, Scanning Microsc. 30 (4) (2008) 324–330.

[5] F. Donatini, A. de Luna Bugallo, P. Tchoulfian, G. Chicot, C. Sartel, V. Sallet, J. Pernot, Comparison of three e-beam techniques for electric field imaging and carrier diffusion length measurement on the same nanowires, Nano Lett. 16 (5) (2016) 2938–2944.

[6] R. Guo, T. Walther, Towards quantification of doping in gallium arsenide nanostructures by low-energy scanning electron microscopy and conductive atomic force microscopy, J. Microsc. (2024).

[7] G. Jayakody, T. Wells, M. El-Gomati, Imaging of doped si in low and very low voltage sem: the contrast interpretation, J. Electron. Spectros. Relat. Phenomena 143 (2–3) (2005) 233–239.

[8] E. Kieft, E. Bosch, Refinement of Monte Carlo simulations of electron–specimen interaction in low-voltage sem, J. Phys. D: Appl. Phys. 41 (21) (2008) 215310.

[9] K. Zhang, C.-G. Ban, Y. Yuan, L. Huang, Optimized dopant imaging for gan by a scanning electron microscopy, J. Microsc. 291 (2) (2023) 177–185.

[10] W.D. Rau, P. Schwander, F.H. Baumann, W. Höppner, A. Ourmazd, Two-dimensional mapping of the electrostatic potential in transistors by electron holography, Phys. Rev. Lett. 82 (1999) 2614–2617, http://dx.doi.org/10.1103/PhysRevLett.82.2614, URL http://link.aps.org/doi/10.1103/PhysRevLett.82.2614.

[11] D. Wolf, A. Lubk, A. Lenk, S. Sturm, H. Lichte, Tomographic investigation of fermi level pinning at focused ion beam milled semiconductor surfaces, Appl. Phys. Lett. 103 (26) (2013) 264104, http://dx.doi.org/10.1063/1.4858957.

[12] A. Pantzer, A. Vakahy, Z. Eliyahou, G. Levi, D. Horvitz, A. Kohn, Dopant mapping in thin fib prepared silicon samples by off-axis electron holography, Ultramicroscopy 138 (2014) 36–45, http://dx.doi.org/10.1016/j.ultramic.2013.12.001.

[13] H. Sasaki, S. Otomo, R. Minato, K. Yamamoto, T. Hirayama, Direct observation of dopant distribution in gaas compound semiconductors using phase-shifting electron holography and lorentz microscopy, J. Electron Microsc. 63 (3) (2014) 235–242, http://dx.doi.org/10.1093/jmicro/dfu008.

[14] D. Cooper, F. Bertin, P. Salles, G. Benassayag, Focused ion beam specimen preparation for off-axis electron holography using Si, Ga, and Au ions, Appl. Phys. Lett. 93 (4) (2008) 043510, http://dx.doi.org/10.1063/1.2960351.

[15] D. Cooper, A.C. Twitchett, P.K. Somodi, P.A. Midgley, R.E. Dunin-Borkowski, I. Farrer, D.A. Ritchie, Improvement in electron holographic phase images of focused-ion-beam-milled GaAs and Si Pn junctions by in situ annealing, Appl. Phys. Lett. 88 (6) (2006) 063510, http://dx.doi.org/10.1063/1.2172068.

[16] D. Cooper, C. Ailliot, J.-P. Barnes, J.-M. Hartmann, P. Salles, G. Benassayag, R.E. Dunin-Borkowski, Dopant profiling of focused ion beam milled semiconductors using off-axis electron holography; reducing artifacts, extending detection limits and reducing the effects of gallium implantation, Ultramicroscopy 110 (5) (2010) 383–389, http://dx.doi.org/10.1016/j.ultramic.2010.02.001.

[17] S.R. Alugubelli, H. Fu, K. Fu, H. Liu, Y. Zhao, M.R. McCartney, F.A. Ponce, Determination of electronic band structure by electron holography of etched-and-regrown interfaces in gan pin diodes, Appl. Phys. Lett. 115 (20) (2019) 201602, http://dx.doi.org/10.1063/1.5127014.

[18] N. Ikarashi, T. Ikezawa, K. Uejima, T. Fukai, M. Miyamura, A. Toda, M. Hane, Electron holography analysis of a shallow junction for planar-bulk metal–oxide–semiconductor field-effect transistors approaching the scaling limit, J. Appl. Phys. 103 (11) (2008) 114514, http://dx.doi.org/10.1063/1.2937246.

[19] D. Shindo, Y. Murakami, Electron holography study of electric field variations, J. Electron. Microsc. 60 (suppl_1) (2011) S225–S237, http://dx.doi.org/10.1093/jmicro/dfr017.

[20] J.H. Yoo, J.-M. Yang, S. Ulugbek, C.W. Ahn, W.-J. Hwang, J.K. Park, C.M. Park, S.B. Hong, J.J. Kim, D. Shindo, Electron holography study for two-dimensional dopant profile measurement with specimens prepared by backside ion milling, J. Electron Microsc. 57 (1) (2008) 13–18, http://dx.doi.org/10.1093/jmicro/dfm037.

[21] S. Yazdi, T. Kasama, M. Beleggia, M.S. Yekta, D.W. McComb, A.C. Twitchett-Harrison, R.E. Dunin-Borkowski, Towards quantitative electrostatic potential mapping of working semiconductor devices using off-axis electron holography, Ultramicroscopy 152 (2015) 10–20, http://dx.doi.org/10.1016/j.ultramic.2014.12.012.

[22] M. Gribelyuk, J. Mody, E. Kaganer, S. Furkay, J. Miller, A. Charsky, Sample preparation by focused ion beam without argon ion milling for quantitative electron holography of pn junctions, J. Appl. Phys. 126 (6) (2019) 065702, http://dx.doi.org/10.1063/1.5086797.

[23] M. Beleggia, P.F. Fazzini, P. Merli, G. Pozzi, Influence of charged oxide layers on tem imaging of reverse-biased $p-n$ junctions, Phys. Rev. B 67 (2003) 045328, http://dx.doi.org/10.1103/PhysRevB.67.045328, URL https://link.aps.org/doi/10.1103/PhysRevB.67.045328.

[24] Y. Wang, M. Schnedler, Q. Lan, F. Zheng, L. Freter, Y. Lu, U. Breuer, H. Eisele, J.-F. Carlin, R. Butté, N. Grandjean, R.E. Dunin-Borkowski, P. Ebert, Interplay of anomalous strain relaxation and minimization of polarization changes at nitride semiconductor heterointerfaces, Phys. Rev. B 102 (2020) 245304, http://dx.doi.org/10.1103/PhysRevB.102.245304, URL https://link.aps.org/doi/10.1103/PhysRevB.102.245304.

[25] K. Yamamoto, K. Nakano, A. Tanaka, Y. Honda, Y. Ando, M. Ogura, M. Matsumoto, S. Anada, Y. Ishikawa, H. Amano, et al., Visualization of different carrier concentrations in n-type-gan semiconductors by phase-shifting electron holography with multiple electron biprisms, Microscopy 69 (1) (2020) 1–10, http://dx.doi.org/10.1093/jmicro/dfz037.

[26] Z. Gan, M. Gu, J. Tang, C. Wang, Y. He, K. Wang, C. Wang, D. Smith, M. Mc-Cartney, Direct mapping of charge distribution during lithiation of Ge nanowires using off-axis electron holography, Nano Lett. 16 (6) (2016) 3748–3753, http://dx.doi.org/10.1021/acs.nanolett.6b01099.

[27] H. Sasaki, K. Yamamoto, T. Hirayama, S. Ootomo, T. Matsuda, F. Iwase, R. Nakasaki, H. Ishii, Mapping of dopant concentration in a gaas semiconductor by off-axis phase-shifting electron holography, Appl. Phys. Lett. 89 (24) (2006) 244101, http://dx.doi.org/10.1063/1.2402907.

[28] D. Cooper, R.E. Dunin-Borkowski, Interpretation of phase images of delta-doped layers, Microscopy 62 (suppl_1) (2013) S87–S98, http://dx.doi.org/10.1093/jmicro/dft014.

[29] M. Gribelyuk, M. McCartney, J. Li, C. Murthy, P. Ronsheim, B. Doris, J. McMurray, S. Hegde, D.J. Smith, Mapping of electrostatic potential in deep submicron cmos devices by electron holography, Phys. Rev. Lett. 89 (2) (2002) 025502, http://dx.doi.org/10.1103/PhysRevLett.89.025502.

[30] A. Twitchett, R. Dunin-Borkowski, P. Midgley, Quantitative electron holography of biased semiconductor devices, Phys. Rev. Lett. 88 (23) (2002) 238302, http://dx.doi.org/10.1103/PhysRevLett.88.238302.

[31] Z. Wang, K. Sasaki, N. Kato, K. Urata, T. Hirayama, H. Saka, Examination of electrostatic potential distribution across an implanted p–n junction by electron holography, Microscopy 50 (6) (2001) 479–484, http://dx.doi.org/10.1093/jmicro/50.6.479.

[32] S.M. Allen, E.L. Hall, Foil thickness measurements from convergent-beam diffraction patterns an experimental assessment of errors, Philos. Mag. A 46 (2) (1982) 243–253, http://dx.doi.org/10.1080/01418618208239917.

[33] C. Boothroyd, A. Kovács, K. Tillmann, Fei titan g2 60-300 holo, J. Large-Scale Res. Facilit. 2 (2016) A44, http://dx.doi.org/10.17815/jlsrf-2-70.

[34] K. Ji, M. Schnedler, Q. Lan, F. Zheng, Y. Wang, Y. Lu, H. Eisele, J.-F. Carlin, R. Butté, N. Grandjean, R.E. Dunin-Borkowski, P. Ebert, Identification and thermal healing of focused ion beam-induced defects in gan using off-axis electron holography, Appl. Phys. Express 17 (2024) 016505, http://dx.doi.org/10.35848/1882-0786/ad163d.

[35] M. Schnedler, V. Portz, P. Weidlich, R. Dunin-Borkowski, P. Ebert, Quantitative description of photoexcited scanning tunneling spectroscopy and its application to the gaas (110) surface, Phys. Rev. B 91 (23) (2015) 235305, http://dx.doi.org/10.1103/PhysRevB.91.235305.

[36] M. Schnedler, R. Dunin-Borkowski, P. Ebert, Importance of quantum correction for the quantitative simulation of photoexcited scanning tunneling spectra of semiconductor surfaces, Phys. Rev. B 93 (2016) 195444, http://dx.doi.org/10.1103/PhysRevB.93.195444, URL http://link.aps.org/doi/10.1103/PhysRevB.93.195444.

[37] R.B. Dingle, Scattering of electrons and holes by charged donors and acceptors in semiconductors, Phil. Mag. 7 (46) (1955) 831, http://dx.doi.org/10.1080/14786440808561235.

[38] Ph. Ebert, T. Zhang, F. Kluge, M. Simon, Z. Zhang, K. Urban, Importance of many-body effects in the clustering of charged Zn dopant atoms in GaAs, Phys. Rev. Lett. 83 (4) (1999) 757–760, http://dx.doi.org/10.1103/PhysRevLett.83.757, URL http://link.aps.org/doi/10.1103/PhysRevLett.83.757.

[39] R.E. Dunin-Borkowski, A. Kovács, T. Kasama, M.R. McCartney, D.J. Smith, Springer HandBook of Microscopy, Springer HandBook, Springer, Cham, 2019, pp. 767–818, http://dx.doi.org/10.1007/978-3-030-00069-1, Ch. 16. Electron Holography.

[40] D. Cooper, Off-axis electron holography for the measurement of active dopants in silicon semiconductor devices, J. Phys. D: Appl. Phys. 49 (47) (2016) 474001, http://dx.doi.org/10.1088/0022-3727/49/47/474001.

[41] S. Anada, K. Yamamoto, H. Sasaki, N. Shibata, Y. Hori, K. Kinugawa, A. Imamura, T. Hirayama, Precise measurement of electric potential, field, and charge density profiles across a biased gaas pn tunnel junction by in situ phase-shifting electron holography, J. Appl. Phys. 122 (22) (2017) 225702, http://dx.doi.org/10.1063/1.5006837.

[42] H. Hebal, Z. Koziol, S. Lisesivdin, R. Steed, General-purpose open-source 1d self-consistent Schrödinger-Poisson solver: Aestimo 1d, Comput. Mater. Sci. 186 (2021) 110015, http://dx.doi.org/10.1016/j.commatsci.2020.110015.